DETC2016-60181

A DIGITAL MATERIAL DESIGN FRAMEWORK FOR 3D-PRINTED HETEROGENEOUS OBJECTS

Pu Huang
Epstein Department of Industrial and Systems
Engineering, University of Southern California
Los Angeles, CA, USA

Yongqiang Li
Epstein Department of Industrial and Systems
Engineering, University of Southern California
Los Angeles, CA, USA

Yong Chen*
Epstein Department of Industrial and Systems
Engineering, University of Southern California
Los Angeles, CA, USA

Jun Zeng
Print and 3D Lab, HP Labs, Hewlett-Packard Co.
Palo Alto, CA, USA

*Author of correspondence, Phone: (213) 740-7829, Fax: (213) 740-1120, Email: yongchen@usc.edu

ABSTRACT

In the paper a digital material design framework is presented to compute multi-material distributions in three-dimensional (3D) model based on given user requirements for additive manufacturing (AM) processes. It is challenging to directly optimize digital material composition due to extremely large design space. The presented material design framework consists of three stages. In the first stage, continuous material property distribution in the geometric model is computed to achieve the desired user requirements. In the second stage, a material dithering method is developed to convert the continuous material property distribution into 3D printable digital material distribution. A tile-based material patterning method and accordingly constructed material library are presented to efficiently perform material dithering in the given 3D model. Finite element analysis (FEA) is used to evaluate the performance of the computed digital material distributions. To mimic the layer-based AM process, cubic meshes are chosen to define the geometric shape in the digital material design stage, and its resolution is set based on the capability of the selected AM process. In the third stage, slicing data is generated from the cubic mesh model and can be used in 3D printing processes. Three test cases are presented to demonstrate the capability of the digital material design framework. Both FEA-based simulation and physical experiments are performed; in addition, their results are compared to verify the tile-based material pattern library and the related material dithering method.

KEYWORDS

Digital material, computer-aided design, additive manufacturing, dithering, Stereolithography

1 INTRODUCTION

Additive manufacturing (AM) can use multiple types of materials (e.g. rigid and flexible materials) to fabricate a heterogeneous object with complex shape. Several AM processes with such capabilities have been developed before such as nozzle deposition [1], direct metal deposition [2], and micro droplets dispensing [3]. In our previous work [4], a mask-image-projection based Stereolithography (MIP-SL)

process was also developed to fabricate heterogeneous objects with digitally controlled multi-material deposition. Similar multi-material MIP-SL process has also been used in scaffold fabrication for tissue engineering [5, 6].

In the MIP-SL process, an input three-dimensional (3D) model is sliced into a set of two-dimensional (2D) layers, which are defined as mask images. The generated mask images are then projected onto photocurable resin to selectively solidify related layers that are accumulated to build the designed model. During the layer-based fabrication process, the local material properties of a small region such as stiffness and electrical conductivity can be changed by controlling the material composition of the region. Consequently, an accordingly built heterogeneous object may satisfy complex user requirements by integrating different materials at various places. Hence, in addition to geometric shapes that are commonly used in product design, an object can also use various multi-material compositions to achieve desired design performance. Such fabrication capability provides tremendous design freedom to enable design performances that are difficult or infeasible to be achieved before [7]. However, how to design a heterogeneous object such that it can achieve given design performance and, at the same time, can be fabricated by AM processes is critical yet challenging. Such a problem is the focus of this paper. The AM process considered in our study is the multi-material MIP-SL process [4]; however, the proposed design method is general and can be extended to other AM processes as well.

Figure 1 shows the proposed digital material design framework, in which a 3D model and user's design requirements are used as the input. Based on them, mask images are generated as the output that can be used in the MIP-SL process to fabricate the accordingly designed object. The design requirements considered in this paper are shape deformation under given loads and constrains. The material property that controls the shape deformation of an object is the stiffness of the composition material, which is defined as Young's modulus value. The design framework consists of three stages. In the first stage, a Young's modulus value distribution in the input 3D model is computed to achieve the given design requirements. To speed up the computing process, Finite Element Analysis (FEA) simulation based on volumetric elements such as tetrahedrons is used to optimize the Young's modulus values in a continuous space domain. In the second stage, a N-level material dithering method is used to convert the continuous Young's modulus distribution into discrete material composition that is 3D-printable and has close Young's modulus values. That is, the continuous distribution of material property is approximated by a distribution of two or more types of printable materials. A library of N-level tile-based material patterns is pre-computed to efficiently compute such an approximation. In addition, cubic meshes that mimic the AM processes are used to define the discrete volumetric domain. The resolution of the cubic meshes can be set base on 3D printer's *XYZ* resolutions. In the third stage, slicing data (i.e. mask images for the MIP-SL process) is generated that can be directly used by 3D printers. In addition to Young's modulus, the material property in our design framework can also be others such as electrical conductivity.
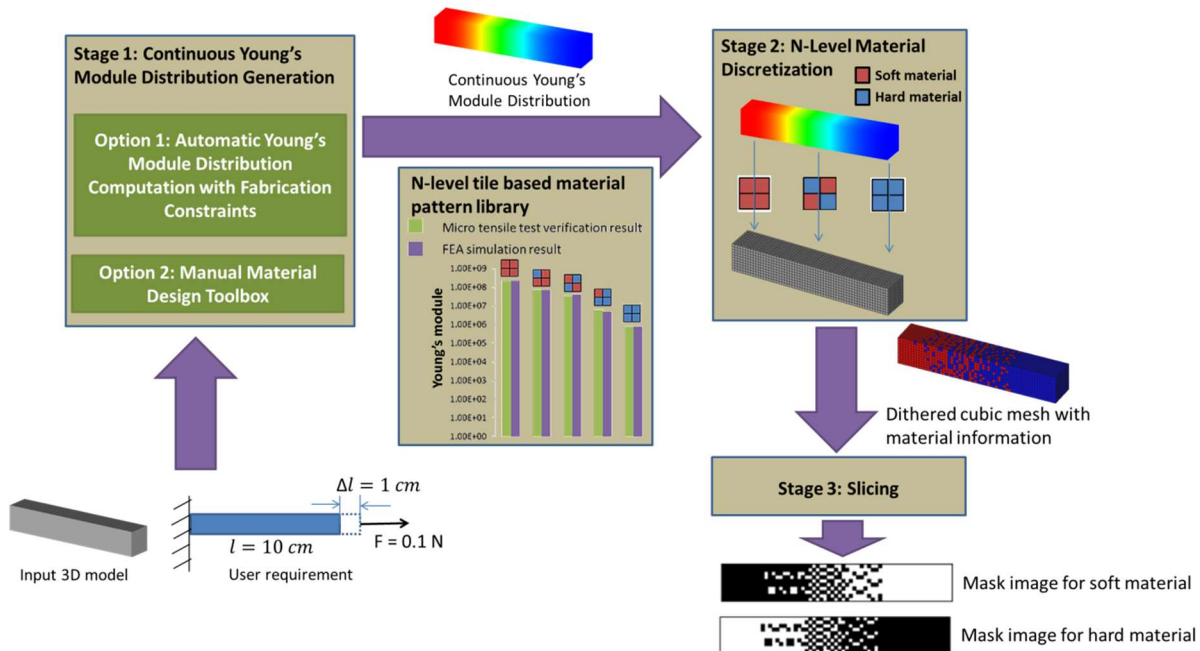

Figure 1. Work flow of the proposed framework.

Hence the digital material design problem considered in this paper can be formulated as follows.

Problem Definition. Consider the cubic mesh of a 3D model with each cubic element corresponding to the smallest feature size that a 3D printer can fabricate. Assume one of N

types of materials can be deposited in each cubic element. If a heterogeneous object based on the given 3D model has a total of n cubic elements. The object will have N^n possible material compositions. And our goal is to compute a composition that can satisfy the given design requirements.

Note that the design space considered in our digital material composition problem is extremely large. For example, for a very simple cubic mesh with $10 \times 10 \times 10$ cubic elements, $n=1000$; accordingly, the number of possible material compositions for 2 types of materials would be $2^{1000} =1e+301$. Consequently, using some brute force approaches to explore such large combinatorial compositions is infeasible. At the same time, search heuristics such as genetic algorithm (GA) are also difficult due to such a large design space. In the paper we present a digital material design approach by first converting the discrete material composition problem into a continuous material property design problem, and then using a heuristic-based material discretization approach to compute discrete material composition based on the continuous material property distribution.

The technical contributions of the paper are highlighted as follows:

- A digital material design framework is presented to compute 3D-printable material composition based on user's design requirements;
- Two computation approaches are identified to compute continuous material property values in a 3D model based on given design requirements;
- A novel N-level material dithering method is presented that can effectively convert continuous material property value into discrete material composition with two or more types of materials;
- A library of tile-based material patterns and pre-computed material properties are presented for the dithering-based material discretization;
- A cubic mesh representation and a related slicing algorithm are developed for the MIP-SL process to generate mask images based on the computed digital material compositions.

The remainder of the paper is organized as follows. Section 2 reviews the related work. Section 3 introduces two computation methods that can be used in generating continuous Young's modulus values in a 3D model based on user's design requirements. Section 4 discusses the tile-based material pattern library and related material properties. Section 5 presents a material dithering algorithm using the pre-computed material pattern library to convert the continuous Young's modulus values into 3D-printable material composition. Section 6 introduces a slicing algorithm to compute mask images that are required by the MIP-SL process. Section 7 presents the experimental results of three test cases. Finally, conclusions are drawn with future work in Section 8.

2 RELATED WORK

Material design based on design requirements
Bickel *et al.* presented an approach to achieve automatic material design driven by user requirements [8, 9]. They firstly

used a sampling based approach to model the mechanical property (Young's modulus) of the available base materials for layered manufacturing. Then a combinatory optimization was used to select base material for each volumetric region. However, the resolution of the volumetric tessellation is very low because the solid will be divided into only several layers. Although the combinatory optimization can give an optimal material distribution among those layers, the result is not accurate due to the low resolution of volumetric optimization domain. If a space domain with high resolution is used, the combinatory optimization will become time consuming due to extremely large design space. Hiller and Lipson [11] presented an approach, in which a 3D model is first tessellated into voxels, and then discrete cosine transform (DCT) is used to reduce the dimension of the optimization domain in order to efficiently conduct the material optimization. In the GA-based approach, FEA is used to evaluate the approximation error during each iteration. Xu *et al.* [10] presented an approach based on material space reduction technique to significantly reduce the optimization space, which makes it feasible to compute material distribution even for high resolution volumetric mesh. In their algorithm, the considered material space is continuous. However, the materials that are available in the layered-based AM processes are usually limited to two or three types of materials. In addition, the volumetric elements used in their algorithm are tetrahedron; it is challenging to convert such a volumetric element into a layered material layout with close material property for 3D printing. Our design framework adopts the approach [10] in the first design stage while addressing the material layout conversion problem in the second design stage (refer to the discussion in Section 3).

Chen *et al.* [12] presented a general framework for 3D printing to convert user specifications to material distribution. Two data structures are designed for the framework. Reducer tree is used to hold the volumetric tessellation and tuner node is used to handle the combinatorial optimization. Widimce *et al.* [13] presented a flexible and parallelized pipeline that imitates the graphics rendering pipeline. No combinatorial optimization is needed in the volumetric domain. Instead, the pipeline takes 3D model and related texture as user input. Accordingly each voxel is processed into 3D-printable material by imitating how graphics pipeline processes each pixel into displayable color. This approach is highly parallelizable and programmable. However, the user input is only limited to appearance. Other material distribution design approaches have also been developed for achieving given appearance requirements based on 3D printing [14, 15]. In addition to using material distribution to achieve given design requirements, many other design methods have been developed for 3D printing by using unit structures to achieve given user specifications [22-28].

Material dithering and half-toning
Dithering and half-toning are well-known techniques for 2D color printing. A dithering algorithm for colored 3D printing was presented in [17] to control local material composition in 3D printing. It converts continuous-tone representation of heterogeneous objects into discrete version of machine

instructions. However, the method mainly focuses on minimizing the color approximation error based on the dispersed-dot ordered dithering approach by Bayer [18]. No FEA evaluation is used on the resultant dithering results. Zhou and Chen [19] presented a 3D half-toning algorithm for a 3D printing process based on ink-jet droplets; however, the approach is not targeting on approximating the mechanical property provided by material distribution in continuous domain. Both of the methods were inspired by the half-toning methods that have been well developed for 2D color printing. Most of the 2D half-toning techniques can be classified into three categories: (1) clustered-dot ordered dithering, (2) dispersed-dot ordered dithering, and (3) dynamic thresholding. Reviews of those half-toning methods can be found in [20-22]. The dithering method used in our design framework is inspired by the dispersed-dot ordered dithering approach; however, instead of visual appearance, we consider the mechanical behavior in the material dithering process, which has different principle from the color appearance in color printing. In our study, the pre-defined dithering patterns are designed based on the isotropic mechanical behavior, and the FEA-based simulation is used to evaluate the mechanical behavior.

3 COMPUTATION OF CONTINUOUS YOUNG'S MODULUS DISTRIBUTION

In the first stage of our design framework, a continuous Young's modulus distribution is computed based on user's design requirements. Two options are available in our design framework to enable a user to compute such material property distribution. The first option is a material property optimization method [10] in which an algorithm is used to convert user's input into a continuous Young's modulus distribution in the given computer-aided design (CAD) model. The second option is a feature-based design method, which allows a user to interactively design the material distribution inside a CAD model [11]. The two options are briefly discussed as follows.

Computation of material property distribution in continuous domain

For a given 3D model with external load and the boundary conditions, the approach presented in [10] can efficiently generate a continuous Young's modulus distribution in the designed object. The idea is to first tessellate the CAD model into a tetrahedron model in order to apply the FEA-based simulation. Then the design problem is formulated as an optimization problem to find the optimal material vector that can best achieve the user specified mechanical response. The problem can be formulated using the following equations:

$$\min_{E,\tilde{u}} \frac{1}{2} E^{T} L E + \frac{\alpha}{2} \|\tilde{f}(E) - \bar{f}\|^{2} + \frac{\alpha\beta}{2} \|\tilde{u} - \bar{u}\|^{2} \qquad (1)$$

where E is the material vector, each of its element being the Young's modulus of a tetrahedron, L is the discrete mesh Laplacian for scalar fields that are defined on the tetrahedron of a mesh (such as E), $\bar{f}$ and $\bar{u}$ are the user specified loading force and displacement, $\tilde{f}$ and $\tilde{u}$ are the loading force and displacement vectors in each iteration of the FEA-based

simulation, and α, β are the weights that define the importance of matching forces and displacements.

The material space (i.e. the space in which material vector E is defined) is continuous and has the dimension n (assume n is the number of tetrahedrons). Since the FEA-based simulation needs to be conducted in each iteration to evaluate the difference between the current mechanical response and the desired mechanical response, the optimization will be extremely slow if a traditional optimization technique such as gradient decent method is used. Model reduction is a well-known technique that can be used to achieve fast deformation simulation [30]. It can dramatically reduce the dimension of the problem with as little error introduced as possible. In [10], the authors adopted model reduction to reduce the dimension of the material space. By applying the transformation E = Bz where B is the material basis matrix, and z is the reduced material vector, E in Equation (1) can be replaced to obtain the optimization problem:

$$\min_{z,\tilde{u}} \frac{1}{2} z^{T} Q z + \frac{\alpha}{2} \|\tilde{f}(E) - \bar{f}\|^{2} + \frac{\alpha\beta}{2} \|\tilde{u} - \bar{u}\|^{2} \qquad (2)$$

where $Q = B^{T} L B$ is the reduced Laplacian matrix. Reducing the dimension of material vector improves the optimization speed by two orders of magnitude and helps it to achieve nearly interactive material design speed.

Figure 2 shows a test result based on the approach [10]. From the input tweezers model and expected mechanical response, the method can generate a continuous Young's modulus distribution. Note that different distributions can be generated for varying specified responses (refer to Figure 2a and 2b). The output of the approach is a tetrahedron mesh, in which each tetrahedron has Young's modulus values defined in a continuous domain.
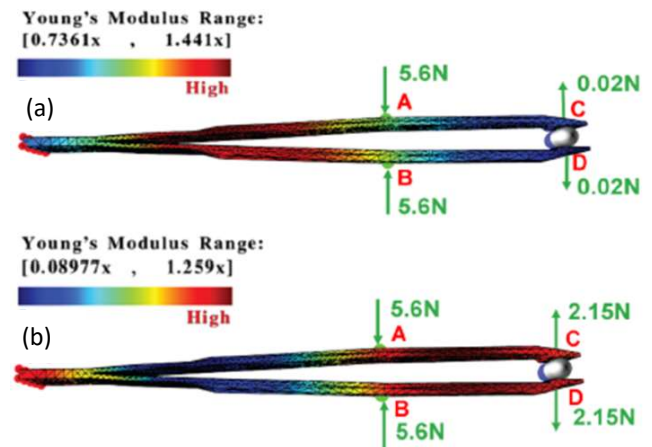

Figure 2. Design of continuous material property of a medical tweezers. Tweezers tetrahedral mesh is loaded with forces at *A* and *B*, so that the tweezers deform and grasp a pill with a normal contact force at *C* and *D*. (a) The spatial distribution of Young's moduli is optimized so that the displacements at *A,B,C,D* remain the same, yet the normal contact force on the pill at *C,D* decreases 20x, to 0.02N. (b) Same as (a), except that the normal contact force is made 5x stronger (2.15N). In the material legend, 1x corresponds to the Young's modulus of aluminum (70GPa).

In our paper the Vega FEA library [35] is used in the FEA-based simulation of all the test cases. Vega is capable of both linear and non-linear simulation with material vector reduction as an option.

Feature based design tool

Our design framework also allows the use of an interactive material design tool to generate or edit the spatial distribution of Young's modulus [11]. The continuous material distribution can be controlled by a set of features. Assume the Young's modulus of two types of materials (soft and hard) are y_{soft} and y_{hard} with $y_{soft} < y_{hard}$. Since the output Young's modulus distribution will be in a continuous range $[y_{soft}, y_{hard}]$, we can use m to represent the normalized material composition value within $[0,1]$ and linearly map it into the interval $[y_{soft}, y_{hard}]$.

In the feature-based material design tool, the control features can be given in any shapes. In our prototype system, four types of control features are defined including point, axis, plane, and line segment. An illustration of the Young's modulus distribution using the four types of control feature and a combined of three control features is shown in Figure 3.
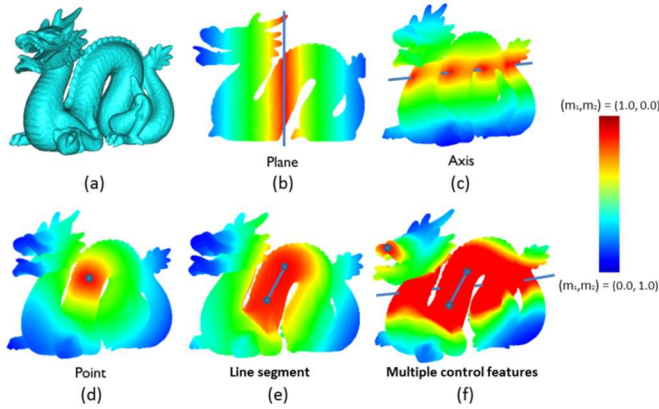
Figure 3. The illustration of designed Young's modulus distribution using different control features. (a) an given CAD model, (b) the plane control feature, (c) the axis control feature, (d) the point control feature, (e) the line segment control feature, and (f) a combination of three control features: line segment, axis and point. Note that the control features are associated with y_{hard}, and the distribution is initialized into 0.0, which indicates y_{soft}.

For any given CAD model M and a point $p \in M$, by defining function $F(u)$, we can have $m_p = F(u_p)$, where u_p and m_p are distance vector and material composition vector associated with p, respectively. Since the distribution is initialized into 0.0 (y_{soft}) and there are r control features associated with 1.0 (y_{hard}). The r-dimensional vector $u_p = (u_{p,1}, u_{p,2}, \ldots \ldots, u_{pr})$ in which $u_{p,i}, i \in [1, r]$ are the minimum distance from p to any material-1 control feature $C_i, i \in [1, r]$. The return vector $m_p = (m_{p,1}, m_{p,2})$ represents the percentage ratio of y_{soft} and y_{hard} at point p. In order words, the material property value at p is calculated by $m_{p,1} \times y_{hard} + m_{p,2} \times y_{soft}$. The function $F(u)$ calculates the percentage $m_{p,1}$ at point p

based on u_p. Then the percentage for background material, material 2 can be calculated simply by $1 - m_{p,1}$. Hence, function F(u) can be represented by the following formula:

$$F(u_p) = \left(f(u_p), 1 - f(u_p)\right) = (m_{p,1}, m_{p,2}) \qquad (3)$$

in which the function $f(u_p)$ is used to calculate $m_{p,1}$. And the function $f(u_p)$ can be defined as follow:

$$f(u_p) = h\left(\sum_{i=1}^{r} g(u_{p,i})\right) \qquad (4)$$

in which $g(u_{p,i})$ is elementary function associated with control feature C_i, which calculates the percentage of material-1 at point p under the influence of the control feature C_i. h(x) is a regulating function that can be defined as:

$$h(x) = \begin{cases} 1 & x > 1 \\ x & x \geq 0 \text{ and } x \leq 1 \\ 0 & x < 0 \end{cases} \qquad (5)$$

It will guarantee the value of $m_{p,1}$ to be in the range of [0, 1]. Hence $m_{p,1}$, the total percentage of y_{hard} at p, is given by the regulated summation of the percentages under all material-1 associated with the control features.

Our prototype system employs a novel way to intuitively define the influence function $g(u_{p,i})$ for control feature C_i. The influence range for C_i is constructed by two areas. The first area is called core area, which has the material property value homogeneously equal to y_{hard} at any point in it. The second area is called the boundary area, in which the percentage of y_{hard} decrease as the distance to C_i becomes larger. The user is free to control the radius of core area around C_i and the radius of boundary area around the core area. In addition, the user can define the transmission function for the boundary area. For example, Figure 4 shows the effect of different radius of core area and boundary area using exponential functions.
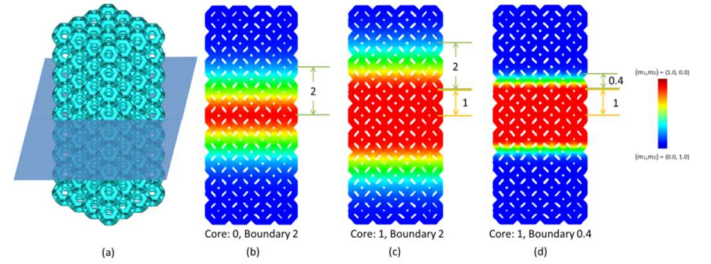

Figure 4. The effect of different radius of core area and boundary area. (a) the truss structure model and the control feature plane, (b) the core radius is 0 and the boundary radius is 2, (c) the core radius is 1 and the boundary radius is 2, (d) the core radius is 1 and the boundary radius is 0.4. The spatial distribution of Young's modulus values is shown in colors between y_{soft} and y_{hard}.

Cubic mesh generation based on fabrication constraints

There are two major reasons that prevent the continuous material property distribution being directly achievable in 3D printing. The first reason is that the number of available materials is limited for a 3D printer. It is impractical to print each dot (or small region) with the desired material property that is given in the continuous material property distribution. In

our digital material design framework, this issue is resolved by using our N-level tile-based material pattern design (refer to Section 4). The second reason is that in 3D printing, the material dot that can be printed is in specific shape, and the material property is homogeneous within it. The material dot of a 3D printer is usually a rectangular cell. Assume the building direction is along the Z axis. The X and Y dimensions of the cell equal to the minimal feature sizes of the AM process in the XY plan, and the Z dimension of the cell equals to its minimum layer thickness in the Z axis. In our study we assume the Z dimension equals to the X and Y dimension for simplicity. Hence each cell considered in the paper would be a cube (as a voxel); however, our method can also be extended to more general cell shapes and sizes.

A solid voxelization method such as [31, 32] can be used to convert an input surface mesh into a uniform cubic model. In our prototype system, we first convert the surface mesh into a LDNI model [33]. This makes the cubic mesh generation rather efficient since the in/out classification of each cube can be easily determined. Figure 5 shows the generated uniform cubic mesh for a given buddy model in STL format.
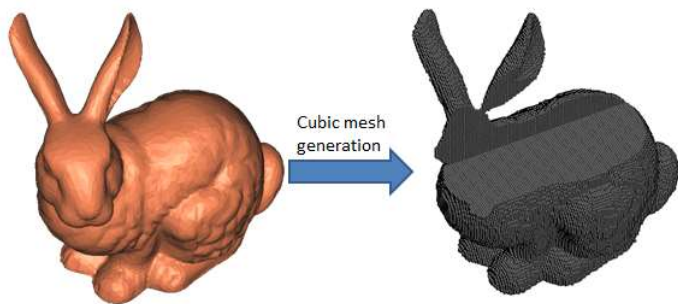

Figure 5. Cubic mesh generation from a surface model.

4   TILE-BASED MATERIAL PATTERN DESIGN

Two computation approaches to generate a continuous Young's modulus distribution were discussed in Section 3. However, the spatial distribution of Young's modulus is in continuous domain and cannot be directly printed using a 3D printer. How to use printable materials given by a 3D printer to closely approximate the computed Young's modulus distribution is an open question that still requires significant effort.

The basic approach used in our digital material design framework is to compose cubic-based tiles based on pre-defined material patterns to build a digital material library such that various Young's modulus values between [Y_{soft}, Y_{hard}] can be achieved. Note that a cubic element in a tile corresponds to the smallest material dot that a 3D printer can fabricate. In our implementation based on the MIP-SL process, such a cubic element is ~0.1mm. Our tile-based material pattern design idea was inspired by the half-toning method that has been developed for 2D color printing. To display a gray-scale image, a tile in 2D printing is designed by using two basic elements (i.e. black and white dots). Similarly, we can use two types of materials (e.g. hard and soft materials) to form different distribution patterns such that the constructed tiles can achieve desired Young's modulus values. Figure 6(a) shows an example of

various 2×2 tiles. By changing the material pattern of how soft and hard materials are used in the tile layout, five different Young's modulus values can be achieved by the 2×2 tiles. Suppose the Young's modulus values of the soft and hard materials are 7.79e5 Pa and 2.31e8 Pa, respectively. The FEA-based simulation can be used to predict the Young's modulus of the tensile bars that are consisted of the three new tiles. Accordingly, a material pattern library as shown in Figure 6(a) can be constructed.
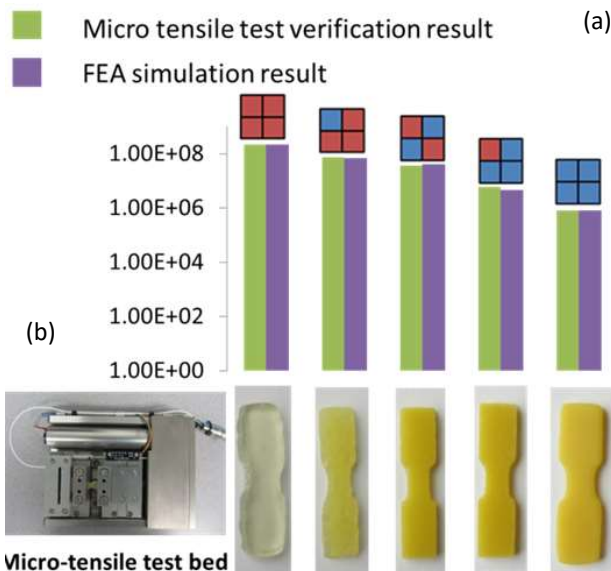

Figure 6. A material pattern library based on 2×2 tiles. (a) An illustration of different material patterns and the related Young's modulus values; (b) a comparison between physically tested Young's modulus and FEA-simulated Young's modulus. From left to right, the material composition changes progressively from soft to hard.

Concept validation

A systematical material pattern design method is required to convert the continuous Young's modulus distribution into printable material composition that can closely approximate its material property. In order to validate the concept of the tile-

based material pattern design approach, we performed physical experiments to verify the computed Young's modulus based on the FEA simulation for the newly constructed tiles. For the aforementioned 2×2 tiles as shown in Figure 6(a), tensile bars related to the five different material pattern designs were fabricated. Each tensile bar consists of consecutive tiles that are repeated in both *X* and *Y* directions. A tensile test machine was used to measure the Young's modulus values of the fabricated tensile bars. Figure 6(b) shows the tensile testing equipment and the fabricated tensile bars.

Based on the given y_{soft} and y_{hard}, the FEA simulation was used to compute Young's modulus values of the three blended tile configurations. Similar to the physical tensile tests, we fix one end of the tensile bar and apply a loading force F at the other end in the FEA simulation. The displacement Δl_i at each vertex v_i of the loading face can be recorded based on the applied loading force. Accordingly, the Young's modulus of the related tile configuration can be calculated based on the following equations:

$$E_{FEA} = \frac{\sigma}{\varepsilon} \tag{6}$$

$$\sigma = \frac{F}{A} \tag{7}$$

$$\varepsilon = \frac{\frac{\sum_1^n \Delta l_i}{n}}{l} \tag{8}$$

where A is the area of the loading face, n is the total number of vertices on the loading face, and l is the total length of the bar. Figure 6(b) shows a comparison of the experimental testing results with the FEA-based simulation results. The two sets of results correspond to each other well, which verifies the tile-based material pattern design concept.

Tile-based material pattern design methodology

Similar to the 2×2 tiles, a N-level material pattern library is constructed by using different number of cubic elements in a tile and varying material composition patterns. In addition, a constructed tile can be formed in 2D or 3D. A 2D tile with dimension *n* has a total of n^2 cubic elements that all lay inside a single layer. In comparison, a 3D tile with dimension *n* in the three orthogonal directions has a total of n^3 cubic elements. Note that a desired property for the designed tiles is isotropic, i.e., the Young's modulus shown by the tile is independent to the loading directions. Accordingly, for *n*=3, Figures 7 and 8 show all the isotropic 3×3 tile patterns in 2D and 3D, respectively.

Isotropic material pattern design with increased sizes can be applied recursively on 2×2 or 3×3 tiles. In other words, larger tiles can be formed by using the previously designed smaller tiles. Hence a N-level material pattern design method can be developed as follows. Assume starting from level 0, a tile is formed by using cubic elements that correspond to the smallest elements that can be built by a 3D printer. Each cubic element is built using one of the two or more available materials (e.g. soft and hard materials). The tiles as shown in Figures 7 and 8 are all belonged to level-0 tiles. Accordingly, level-1 tiles can be formed using level-0 tiles by picking two

material patterns of level-0 tile as the new input "soft" and "hard" materials. The basis material patterns can be any level-0 tile patterns. Accordingly, the selected level-0 tile patterns can be used to form new level-1 tiles. Figure 9 shows an example of the constructed level-1 material tile patterns. The newly constructed material patterns are all isotropic as well. The process can be repeated recursively to form level-2 tiles until level-*N* tiles.
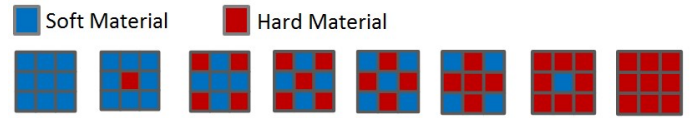

Figure 7. Isotropic patterns for 2D 3×3 tile. Totally there are 8 different isotropic material patterns.
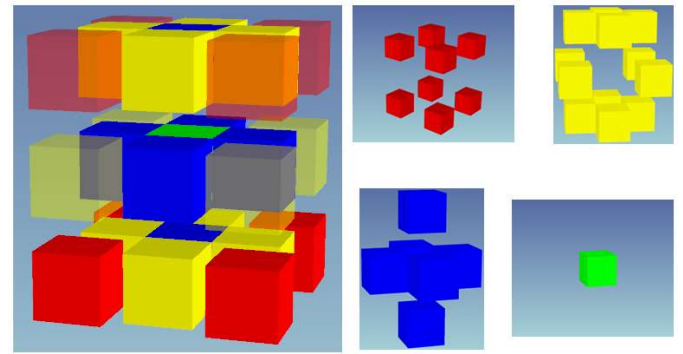

Figure 8. There are a total of 27 elements in the 3D 3×3 tile. They can be classified into four groups. The material type within each group should be the same in order to generate isotropic tile. For each group, they are either all soft or all hard. Hence, there are a total of 2^4=16 different isotropic material patterns for the 3D 3×3 tile.
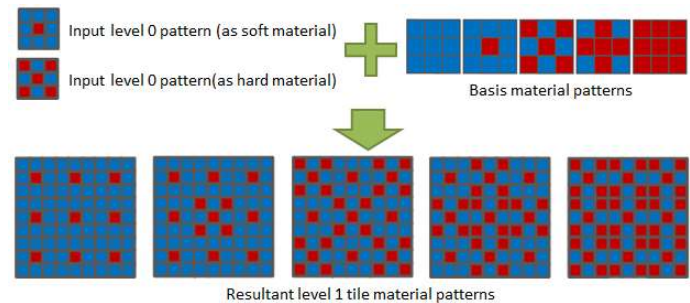

Figure 9. An illustration of how to construct Level 1 tile. By considering two Level 0 tile patterns as "soft" and "hard" material element, we can grow Level 1 patterns using the basis material patterns that are taken from a subset of Level 0 tile patterns.

Note that, in addition to being isotropic, the level-*N* patterns obtained from the aforementioned recursive process always have their Young's modulus values between the Young's modulus values of the two input level-*N*-1 patterns that are used as the "soft" and "hard" materials. Such monotone property on Young's modulus values is important for the newly

Copyright © 2016 by ASME

constructed level-*N* patterns. Such monotone property can be satisfied if the following two conditions are satisfied:

(1) The "soft" level-*N*-1 pattern has a smaller Young's modulus value than the "hard" level-*N*-1 pattern;

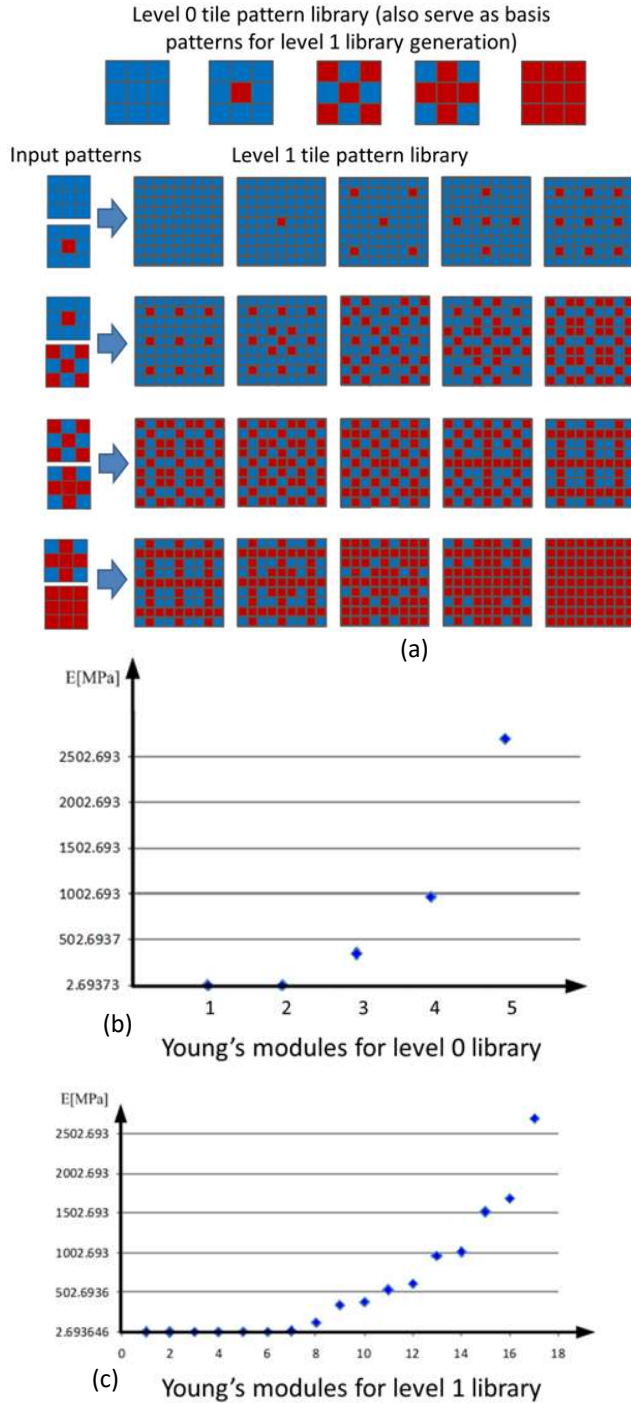(2) The basis material patterns taken from level-0 patterns have monotone property on their Young's modulus values.

(a)

(b)

(c)

Figure 10. The level-0 and level-1 2D tile pattern library and their corresponding Young's modulus values based on the FEA simulation.

Building a N-level tile-based material pattern library

Based on the *N*-level material pattern design method, a material pattern library can be pre-computed to approximate the continuous Young's modulus between those of the soft and hard materials. Figure 10 shows a level-0 library and a level-1 2D tile library that is obtained using the patterns in the level-0 library as the basis and input patterns. In the example, the Young's modulus values of the soft and hard materials are set as 2.69e6 Pa and 2.69e9 Pa, respectively.

Similar to the examples of the N-level tile pattern library in 2D, the presented design method and related library construction procedure can also be used for 3D tiles. Figure 11 is the chart of Young's modulus for level-1 3D tile. Note that, in a level-2 3D tile, there are 27×27×27 unit cubic elements. We can easily achieve a resolution of 126 on Young's modulus values using this level-2 3D tile library.
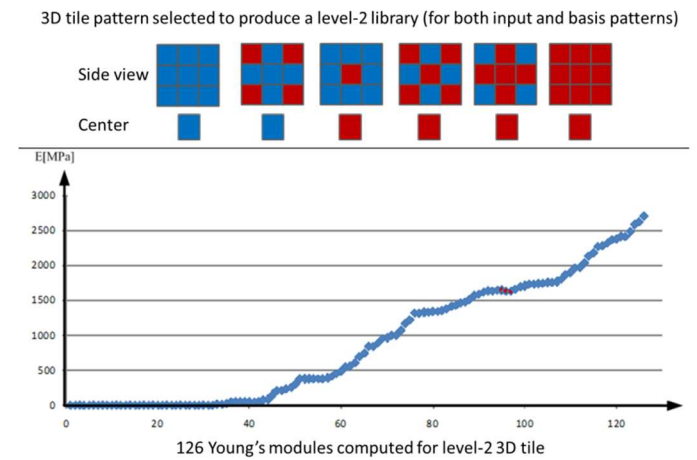

Figure 11. The 6 patterns selected to produce a level-2 3D tile pattern library. There are a total of 126 Young's modulus values as shown in the figure between those of the soft and hard materials.

5 N-LEVEL MATERIAL DISCRETIZATION

Based on the N-level tile pattern library as discussed in Section 4, a material dithering algorithm is developed to efficiently convert the continuous Young's modulus distribution into 3D printable material distribution on the cubic model.

N-level tile-based dithering algorithm

As discussed in Section 3, when computing a cubic model from a given surface model, the size of each cubic element is selected based on the minimal feature size of the used 3D printer. Accordingly, those cubic elements can be organized into a set of tiles. For example, suppose 2×2 2D tiles are used. Figure 12 shows an example of the tiles for a set of given cubic elements. There could be additional cubic elements that cannot be properly organized into a tile. In this case, dummy elements can be added to form a complete tile. Note that these dummy elements will not be considered in the process planning stage. Hence they will not be fabricated in the 3D printing process.
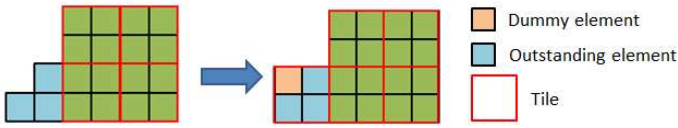
8

Copyright © 2016 by ASME

Figure 12. Illustration of handling outstanding elements.

After organizing all the cubic elements into a set of tiles, each tile needs to be determined on which material pattern to use to achieve the best approximation of the related Young's modulus value. A simple strategy is to first calculate the designed Young's modulus of each tile; accordingly, a material pattern with the closest Young's modulus value can be selected from the pre-computed material pattern library. To calculate Young's modulus value in each tile, we can integrate all the Young's modulus values inside the volume of the tile, and then divide it by the tile volume. This approach is general and can be applied no matter whether the input continuous Young's modulus distribution is represented using tetrahedron mesh or analytical function. However, the integration approach is computational expensive. In our implementation, a simpler approach is used to evaluate the Young's modulus value of each tile. The more efficient heuristic used in our study is to estimate a tile's Young's modulus based on the average of Young's modulus values in all the cubic elements of the tile. The Young's modulus value of each cubic element can be evaluated using its centroid point as a representative although more sampling points in the element can be used as well.

Choosing the closest material pattern to approximate the desired Young's modulus in each tile is intuitive and simple; however, using more sophisticated methods may achieve more accurate approximation. In our study, we investigated the error diffusion methods that have been widely used in 2D color printing. The basic idea of error diffusion is to evaluate the approximation error of each tile, and to spread the error to its neighboring tiles such that their desired Young's modulus values can be adjusted accordingly.

There are many error diffusion methods. Instead of spreading error with constant weight ratio (e.g. Floyd and Steinberg weights [34] as shown in Figure 13a), we derived a new error spreading method that is more suitable for material dithering based on Young's modulus. For simplicity, consider the loading force is given on orthogonal directions. For example, the four tiles, $T_1 - T_4$, are shown in Figure 13. Figure 13(b) demonstrates how T_1 spread its error to T_2 and T_3; and Figure 13(c) shows how T_4 receives error spread from both T_2 and T_3. Starting from T_1, since it is the first element, its desired Young's modulus value E_1 will not be adjusted by the errors received from its neighbors. We can directly pick the material pattern that has the closest Young's modulus to E_1 from the N-level material pattern library. Suppose the related tile now has the Young's modulus $\overline{E1}$. Tile T_2 will be somehow influenced by the error between E_1 and $\overline{E1}$. Hence its desired Young's modulus will be adjusted from E_2 to E2′ accordingly. We found that the adjusted Young's modulus E2′ of T_2 need to follow the physical governing equation:

$$l\frac{\sigma}{E1} + l\frac{\sigma}{E2} = l\frac{\sigma}{\overline{E1}} + l\frac{\sigma}{E2'} \qquad (9)$$

where l is the edge length of a tile, σ is the stress provided by the horizontal force. Hence $l\frac{\sigma}{E1} + l\frac{\sigma}{E2}$ is the desired elongation that tiles T_1 and T_2 are supposed to provide together, and $l\frac{\sigma}{\overline{E1}} + l\frac{\sigma}{E2'}$ is the elongation provided by T_1 and T_2 after E_1 is approximated by $\overline{E1}$ and E_2 adjusted to be new desired Young's modulus E2′. We can easily calculate E2′ because E_1, $\overline{E1}$, E_2 are all known variables. We will eventually choose a material pattern whose Young's modulus is closest to E2′ when we handle T_2. The same principle applies in both horizontal and vertical directions. Since the error only spread rightward or downward, T_2 and T_3 will only be influenced by T_1. And T_4 presents a more general case because it has to consider the errors spread from both T_2 and T_3.
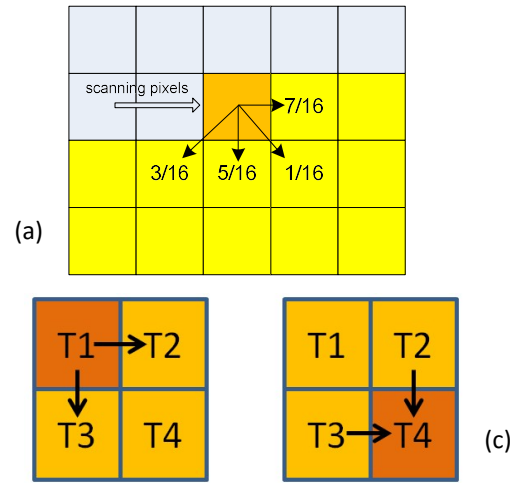

Figure 13. Error diffusion methods. (a) Floyd and Steinberg method; (b) error spreading directions; and (c) error receiving directions.

Assume the material patterns chose for T_2 and T_3 have the Young's modulus $\overline{E2}$ and $\overline{E3}$, respectively. Given Equation (9), for both horizontal and vertical directions, we can compute the adjusted Young's modulus for T_4. This means that we will have an over-constrained system, in which the E4′ value for the horizontal and vertical directions is not the same. We resolve this conflict by taking average of the elongation that E4′ is supposed to provide in both directions. The governing equation is given as follows.

$$l\frac{\sigma}{E4'} = \frac{1}{2}\left[\left(l\frac{\sigma}{E2'} + l\frac{\sigma}{E4} - l\frac{\sigma}{\overline{E2}}\right) + \left(l\frac{\sigma}{E3'} + l\frac{\sigma}{E4} - l\frac{\sigma}{\overline{E3}}\right)\right] \qquad (10)$$

with E2′, $\overline{E2}$, E3′, $\overline{E3}$ and $\overline{E3}$ all known, we can solve E4′ using equation (10). Accordingly, the material pattern whose Young's modulus is the closest to E4′ can be chosen for T_4. In Section 7, we reported the performance of different error diffusion methods including our error diffusion approach and the approach based on Floyd and Steinberg weights for error spreading.

Copyright © 2016 by ASME

Discussion on tile dimension selection

By comparing the tensile test results as shown in Figure 16, it can be observed that the approximations of both 2×2 and 3×3 tiles are significantly better than those of 1×1 tiles (i.e. using constant threshold). This result verifies that, in generally, the more Young's modulus values that a tile can represent, the better approximation can be expected. However, it may not always be appropriate to enlarge the tile size in order to achieve more Young's modulus values in the *N*-level material library. Notice that there exists a trade-off between the resolution of the tile within an object and the Young's modulus resolution that a tile can represent. For example, if 2×2 tile is selected, there will be 5 different Young's modulus in level-0. If 3×3 tile is selected, there will be 8 Young's modulus available in level-0. However, for the same cubic meshes with the finest printing resolution, the number of tiles if 2×2 tiles are used will be 1.5 times larger than that of 3×3 tiles, which will give the dithering algorithm more degree of freedom to conduct the approximation.

We also investigate how the tile size influences the dithering performance by comparing the tensile test results between 2×2 and 3×3 tile (refer to Figure 16). It can be observed from Figure 16 that the 2×2 tiles provide better approximation result. This observation is not expected given that 3×3 tiles has eight Young's modulus values and 2×2 tile has only five Young's modulus values. However, after further investigation, it is identified that the Young's modulus related to the 2×2 tiles has finer resolution in the relatively soft region than that of 3×3 titles (refer to Figure 14). The elongation performance in the tensile test is dominated by the soft materials, which explains why the 2×2 tiles have a better approximation result than the 3×3 tiles.
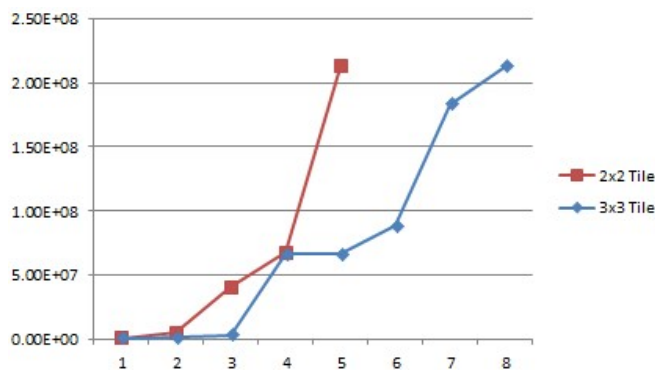

Figure 14. Young's modulus plot for 2×2 level-1 tile and 3×3 level-1 tile. Although they share the same Young's modulus range, the 2×2 tile gives more resolution in the relatively soft region.

In summary, although the tiles with larger Young's modulus resolution tend to provide better approximation, there exists a trade-off between the Young's modulus resolution and the total tile number inside the heterogeneous object. In addition, how the Young's modulus is spread in the range of soft materials should be considered in order to select proper tile design for specific applications.

6 PROCESS PLANNING FOR THE MIP-SL PROCESS

In the multi-material MIP-SL process, one mask image is used to define the shape of one type of materials. Assumption two materials (i.e. soft and hard materials) are available in the MIP-SL based 3D printer. Each layer will need two mask images to build the two types of materials in each layer. In principle, the union of the two mask images for one layer should be the cross section image of the CAD model on this layer (refer to Figure 15). Hence for an input CAD model, two sets of mask images L_1 and L_2 are prepared after slicing the model into a set of layers, with L_1 for soft material and L_2 for hard material.

After getting the cubic mesh, it is trivial to generate the mask images since each cubic cell in the mesh is already corresponding to the minimal feature that can be built by the MIP-SL based 3D printer. We can easily create mask images on each layer and "fill in" pixels on each mask image according to the cubic elements and their corresponding materials. Based on our experiments using our prototype MIP-SL system, the minimal feature that can be safely built is corresponding to a block consisting of 15×15 pixels in our system. So for each cubic element, we fill in 15×15 pixels in the mask image for its material type as illustrated in Figure 15.
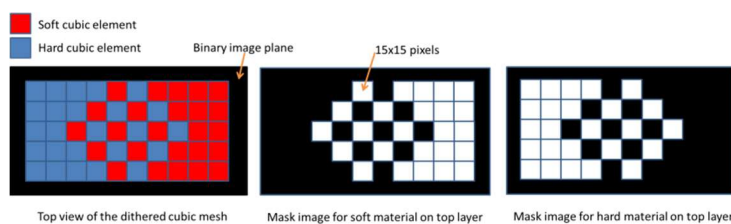

Figure 15. Illustration of the slicing algorithm.

7 TESTING RESULTS

Three test cases are used to test the developed digital material design framework.
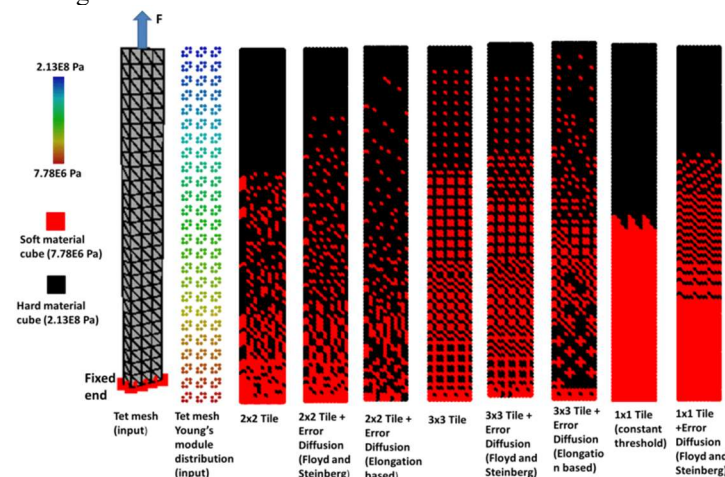

Figure 16. Input tet-mesh and its Young's modulus distribution (each dot represent a tetrahedron and its Young's modulus is indicated by color). All the dithering results are shown with each dot representing a cube in the cubic mesh.
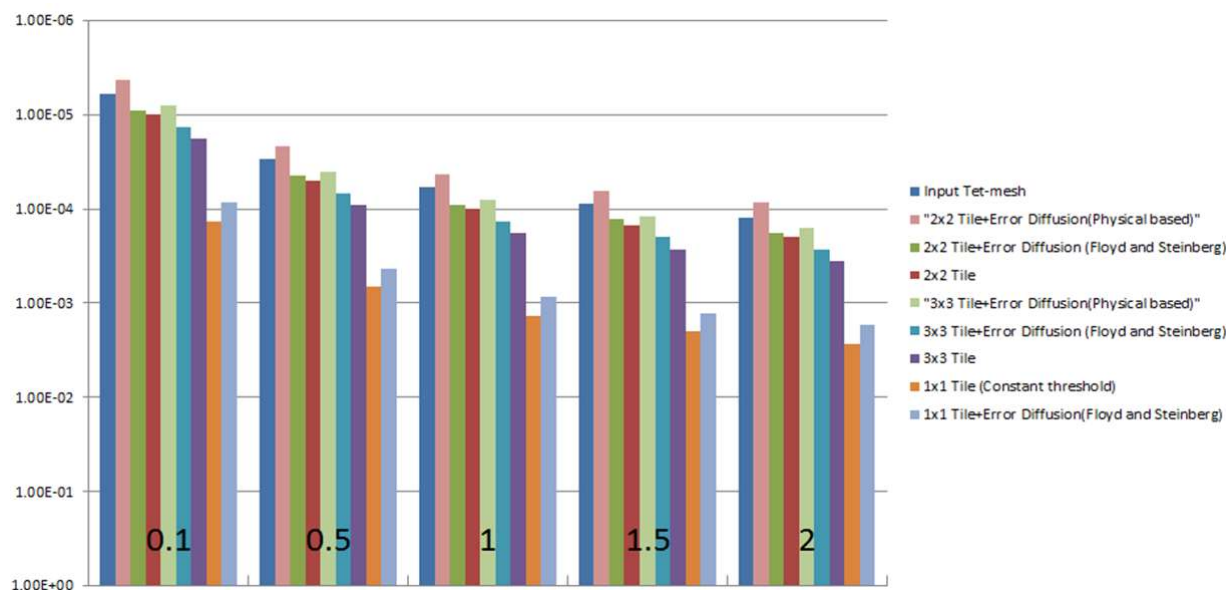
Copyright © 2016 by ASME

Figure 17. The elongation Δl of the tensile test for different dithering settings.
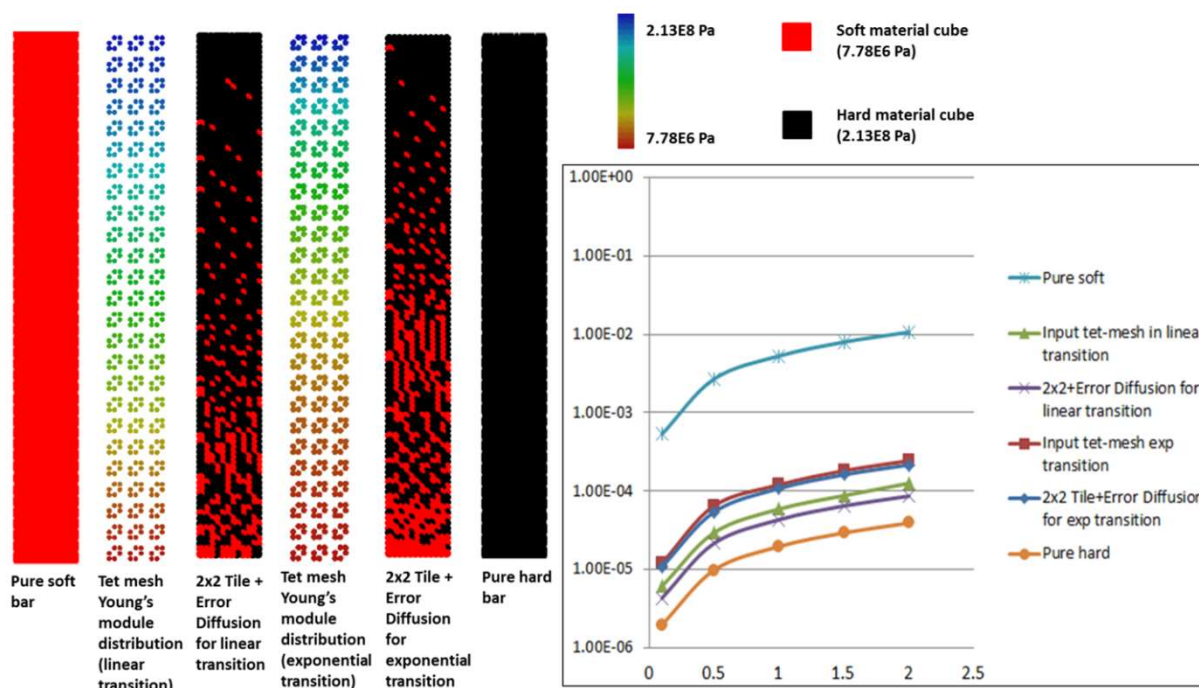

Figure 18. Approximation performance for different input continuous Young's modulus distribution.

Test case 1: A tensile bar

The first test case is a simple tensile bar as shown in Figure 16. The dimension of the tensile bar is 6mm×50mm×2mm. The dimension of each cubic element in the generated cubic mesh is 0.5mm. Hence the cubic mesh resolution is 12×100×4 or 4,800 elements. The boundary condition of the tensile test is represented in Figure 16. The soft end of the bar is fixed while a vertical tensile force is applied at the hard end. The force is increased 4 times from 0.1N to 2.0N. Elongation of the hard

end is recorded as the results, which are shown in Figure 17. The FEA-based simulation using Vega library is conducted on both the input tetrahedron mesh and all the resultant cubic meshes from different dithering settings. The material distributions of the input tet-mesh and resultant dithered cubic mesh are shown in Figure 16. The input tet-mesh has a continuous Young's modulus distribution and its elongation is used as the target of the approximation. We tried three different tile settings, 1×1 tile, 2×2 tile level-0, and 3×3 tile level-0. We

Copyright © 2016 by ASME

also added the error diffusion into our dithering approach. We implemented both the error diffusion method used in displaying half toning (Floyd and Steinberg), and our newly derived tensile-based error diffusion method. In Section 5.2, the tile selection by comparing the results of 1×1, 2×2 and 3×3 tiles has been discussed.

Another comparison we made is the tensile testing performance of the error diffusion methods. We can see from Figure 17 that the material dithering results based on error diffusion methods (no matter which kind of error diffusion methods) have better approximations on the target elongation than without using it. After further comparison, we can see that our tensile-based error diffusion method gives a closer approximation than the Floyd and Steinberg method for both 2×2 and 3×3 tiles.

For the tensile test case, we also evaluated the performance of our material dithering algorithm on approximating different continuous Young's modulus distribution in the input tet-mesh. In Figure 18, we generated dithering results for two different types of continuous Young's modulus transition within the input tet-mesh (i.e. linear transition and exponential transition). We used 2×2 level-0 tile with the tensile-based error diffusion for the dithering process. As a benchmark, we also provided the FEA responses of pure soft and pure hard bars. As can be seen in Figure 18, our tensile-based material dithering method is highly effective in approximating different continuous Young's modulus distributions. Note that, in Figure 18, the exponential scale is used for the Y-axis values, which are the elongation recorded at the loading end of the bar.
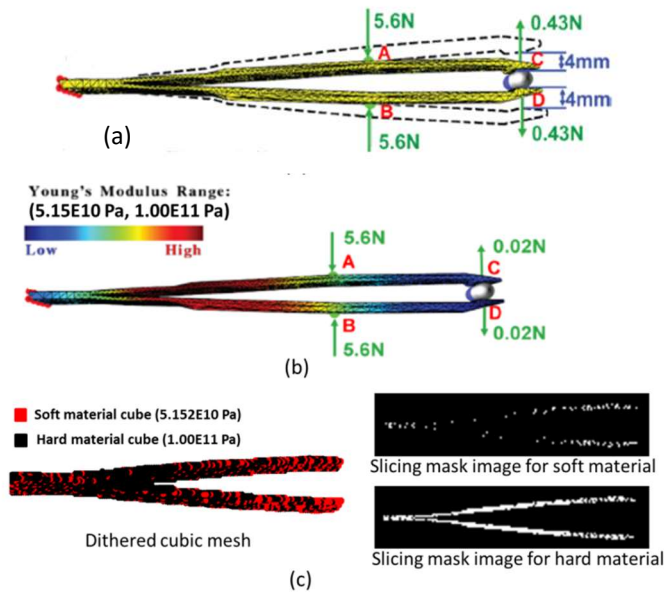

Figure 19. The dithering result of a long tweezers model.

Test case 2: A long tweezers
We applied our digital material design framework to test the tweezers design as shown in Figure 2. Figure 19(a) shows a pure aluminum tweezers' clipping force on the capsule. Figure 19(b) shows the continuous Young's modulus distribution in order to largely reduce the clipping force to only 0.02N [10].

Figure 19(c) shows the dithered cubic mesh based on the given continuous Young's modulus distribution as shown in Figure 19(b). In addition, Figure 19(c) also shows the slicing mask images on a layer for the multi-material MIP-SL process. In this test case, we used 2×2 level-1 tile in the dithering approach. The continuous Young's modulus distribution within the tet-mesh is generated using the approach presented in [10]. As can be seen, the input tet-mesh with continuous Young's modulus is converted into a cubic mesh with all the necessary material compositions that are ready for the 3D printing process.

Test case 3: A short tweezers
In test case 2, the continuous Young's modulus distribution is generated by the material space reduction method as discussed in Section 3.1. Another tweezers test case that we conducted is based on the continuous Young's modulus distribution generated by the feature-based material design tool as discussed in Section 3.2.

Figure 20 shows the short tweezers test case. The dimensional size of the tweezers model is 30mm×18mm×8mm. In this tweezers design, we used three point-based control features to indicate where the part needs to be soft. Accordingly, a continuous Young's modulus distribution can be generated by the feature-based design tool. After the FEA simulation, the designer can further edit the continuous material distribution until a satisfactory design performance is obtained. Based on the designed material distribution, a level-1 2x2 tile library is used in material dithering; each cubic element's dimension is set as 0.5mm. Our dithering method generates a cubic model that carries 3D printable material information. Accordingly, the cubic mesh can be sliced into binary images for each layer as discussed in Section 6. Figure 20 shows the mask images of a layer for both soft and hard materials. The 3D-printed object using our prototype MIP-SL system is shown in Figure 20.
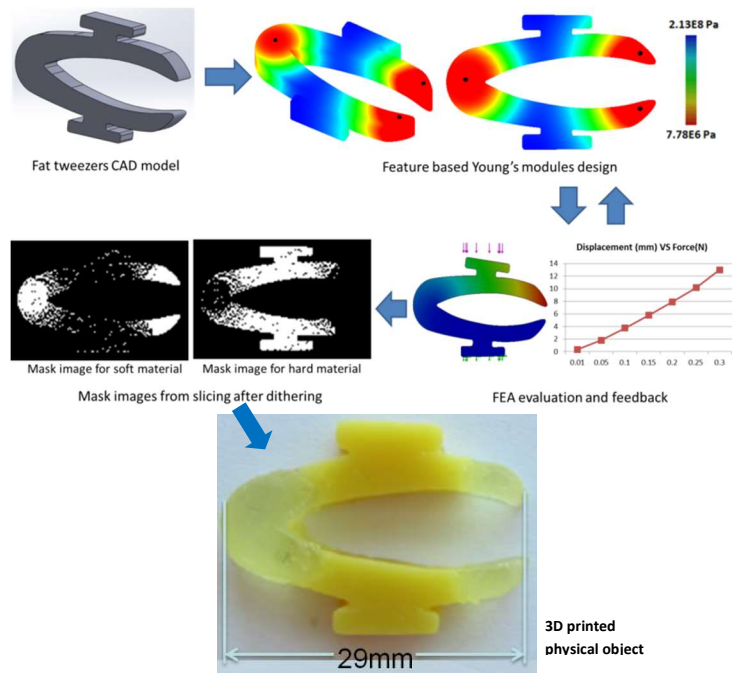

Figure 20. The design and fabrication of a short tweezers.

Copyright © 2016 by ASME

8 CONCLUSIONS

The paper presents a digital material design framework that can compute 3D-printable material distribution for given component shape and design requirements. A user can specify the response of the CAD model under certain loads and constrains. Accordingly, the slicing data to fabricate a multi-material heterogeneous object will be generated by our design framework to closely achieve the given design requirements. The presented digital material design framework consists of three stages. In the first stage, a continuous material property distribution is computed to achieve the given design requirements. In the second stage, a material dithering method is used to convert the continuous material property distribution into discrete 3D-printable material compositions. A material pattern library based on *N*-level tiles has been developed to efficiently compute close material approximation based on the presented material dithering method. A cubic model with its resolution chosen based on 3D printers is used in the material dithering process. In the third stage, slicing data for the selected 3D printing process is generated. Physical experiments have been performed to verify the developed N-level material pattern library. Three test cases have also been presented to illustrate the effectiveness of the developed design framework.

Digital material design for 3D printing processes is a challenging problem due to its extremely large design space. In our future research, further investigation will be conducted to improve the approximation accuracy of the dithering method. Some approaches such as adopting more material patterns and more sophisticated error diffusion techniques will be investigated. In addition, we plan to test the digital material design framework on other material properties other than mechanical responses.

ACKNOWLEDGMENTS

REFERENCES

[1] Hu Y., Blouin V. Y., Fadel G. M., Incorporating manufacturability constraints into the design process of heterogeneous objects, Intelligent Sys. in Design and Manu., Proceedings of the SPIE, 5605, 214-225, 2004.

[2] Hejimadi U. and McAlea K., Selective Laser Sintering of Metal Molds: The RapidTool Process, Solid Freeform Fabrication Symposium, Texas, August 12th-14th, 1996.

[3] Zhu Y. F, Peng C., Yang J. Q. and Wang C. M., An Integrated Design and Fabrication Approach for Heterogeneous Objects, Advanced Materials Research, 383, 5810-5817, 2011

[4] Zhou C., Chen Y., Yang Z., Khoshnevis B., Digital material fabrication using mask-image-projection-based stereolithography." Rapid Prototyping Journal, 19, 3, 2013.

[5] Han L. H., Suri S., Schmidt C. and Chen S., Fabrication of three-dimensional scaffolds for heterogeneous tissue engineering, Biomedical Microdevices, 12(4), 721-725, 2010.

[6] Lee S. A., Chung S. E., Park W. et al., Three-dimensional fabrication of heterogeneous microstructures using soft membrane deformation and optofluidic maskless lithography, Lab Chip, 9(12), 1670-1675, 2009.

[7] Kou X. Y. and Tan S. T., Heterogeneous object modeling: A review, Computer-Aided Design, 39(4), 284-301, 2007.

[8] Bickel B., Bacher M., Otaduy M. A., Matusik W., Pfister H., and Gross M.. 2009. Capture and modeling of non-linear heterogeneous soft tissue. ACM Trans. Graph. 28, 3, Article 89 (July 2009).

[9] Bickel B., Bacher M., Otaduy M. A., Lee H. R., Pfister H., Gross M., and Matusik W., 2010. Design and fabrication of materials with desired deformation behavior. ACM Trans. Graph. 29, 4, Article 63 (July 2010).

[10] Xu H., Li Y., Chen Y., and Barbic J., Interactive Material Design Using Model Reduction, ACM Transactions on Graphics, 34, 2, Article 18, 2015.

[11] Huang P., Deng D., and Chen Y., Modeling and Fabrication of Heterogeneous Three-dimensional Objects based on Additive Manufacturing." International Mechanical Engineering Congress and Exposition, IMECE2013-65724, San Diego, CA, Nov. 15 ~ 21, 2013.

[12] Hiller J. D. and Lipson H., Design Automation for Multi-Material Printing, Solid Freeform Fabrication Symposium, Texas, 2009.

[13] Chen D., Levin D. I. W., Didyk P., Sitthi-Amorn P. and Matusik W., Spec2Fab: A reducer-tuner model for translating specifications to 3D prints, ACM Trans. Graph. 32, 4, Article 135 (2013), 10 pages.

[14] Widimce K., Wang S.P., Ragan-Kelley J., and Matusik W., OpenFab: A Programmable Pipeline for Multi-Material Fabrication, ACM Trans. Graph. 32, 4, Article 136 (2013).

[15] Wetzstein G., Lanman D., Heidrich W. and Raskar R., Layered 3D: Tomographic Image Synthesis for Attenuation-based Light Field and High Dynamic Range Displays, ACM Trans. Graph. 30, 4, 2011, 11 pages.

[16] Holroyd M., Baran I., Lawrence J. and Matusik W., Computing and Fabricating Multilayer Models, ACM Trans. Graph. 30, 6, 2011, 8 pages.

[17] Cho W., Sachs E. M., Patrikalakis N. M. and Troxel D. E., A Dithering Algorithm for Local Composition Control with Three-dimensional Printing, Computer-Aided Design, 35 (9), 851-867, 2003.

[18] Bayer B. E., An Optimum Method for Two Level Rendition of Continuous Tone Pictures, International Conference on Communications, 1973.

[19] Zhou C. and Chen Y., Three-dimensional Digital Halftoning for Layered Manufacturing based on Droplets, Transactions of the North American Manufacturing Research Institution of SME, Vol. 37, p. 175-182, 2009.

[20] Ulichney R., Digital Halftoning, MIT Press, Cambridge, 1987.

[21] Stoffel J. C. and Moreland J. F., A Survey of Electronic Techniques for Pictorial Reproduction, IEEE Transactions on Communications, 19: 1898-1925, 1981.

[22] Jarvis J. F., Judice C. N. and Ninke W. H., A Survey of Techniques for the Display of Continuous-tone Pictures on Bilevel Display, Computer Graphics and Image Processing, 5:13-40, 1976.

[23] Wang H. V., Chen Y., Rosen D. W., A Hybrid Geometric Modeling Method for Large Scale Conformal Cellular Structures, ASME IDETC/CIE 2005 Conference, 25th Computers and Information in Engineering Conference, Long Beach, CA, 2005.

[24] Wang H. V., A Unit Cell Approach for Lightweight Structure and Compliant Mechanism, PhD Dissertation, School of Mechanical Engineering, Georgia Institute of Technology, Atlanta, GA, 2005.

[25] Chen Y., A Mesh-based Geometric Modeling Method for General Structures, ASME IDETC/CIE 2006 Conference, 26th Computers and Information in Engineering Conference, Philadelphia, PA, 2006.

[26] Pasko A., Fryazinov O., Vilbrandt T., Fayolle P., Adzhiev V., Procedural function-based modelling of volumetric microstructures, Graphical Models, 73(5), 2011.

[27] Chen Y., 3D Texture Mapping for Rapid Manufacturing, Computer-Aided Design and Applications 4 (6), 2007.

[28] Chu C., Graf G. and Rosen D. W., Computer Aided Design for Additive Manufacturing of Cellular Structures, Computer-Aided Design and Applications 5 (5), 2007.

[29] Schumacher C., Bickel B., Rys J., Marschner S., Daraio C., Gross M., Microstructures to control elasticity in 3D printing, ACM Transactions on Graphics, 34, 4, 2015, Article No. 136.

[30] Barbic, J. and James, D. L., Real-time Subspace Integration for St. Venant-Kirchhoff Deformable Models. ACM Trans. on Graphics (SIGGRAPH 2005) 24, 3, 982–990, 2005.

[31] Fang S. and Chen H., Hardware Accelerated Voxelization, Computers & Graphics, 24(3), 433-442, 2000.

[32] Eisemann E. and Decoret X., Single-pass GPU Solid Voxelization for Real-time Applications, Proceedings of Graphics Interface, 73-80, 2008.

[33] Chen Y., Wang C. C. L., Layer Depth-Normal Images for Complex Geometries - Part I: Accurate Modeling and Adaptive Sampling, Proceedings of ASME Design Engineering Technical Conferences, 2008.

[34] Floyd R. W. and Steinberg L., An adaptive algorithm for spatial grey scale. Proceedings of the Society of Information Display 17, 75–77, 1976.

[35] J. Barbic, F. S. Sin, D. Schroeder: Vega FEM Library. 2012. http://www.jernejbarbic.com/vega.